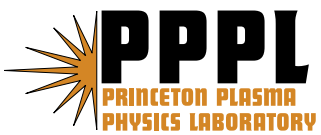

Princeton Plasma Physics Laboratory

PPPL-

PPPL-



Prepared for the U.S. Department of Energy under Contract DE-AC02-76CH03073.

Princeton Plasma Physics Laboratory

Report Disclaimers

Full Legal Disclaimer

This report was prepared as an account of work sponsored by an agency of the United States Government. Neither the United States Government nor any agency thereof, nor any of their employees, nor any of their contractors, subcontractors or their employees, makes any warranty, express or implied, or assumes any legal liability or responsibility for the accuracy, completeness, or any third party's use or the results of such use of any information, apparatus, product, or process disclosed, or represents that its use would not infringe privately owned rights. Reference herein to any specific commercial product, process, or service by trade name, trademark, manufacturer, or otherwise, does not necessarily constitute or imply its endorsement, recommendation, or favoring by the United States Government or any agency thereof or its contractors or subcontractors. The views and opinions of authors expressed herein do not necessarily state or reflect those of the United States Government or any agency thereof.

Trademark Disclaimer

Reference herein to any specific commercial product, process, or service by trade name, trademark, manufacturer, or otherwise, does not necessarily constitute or imply its endorsement, recommendation, or favoring by the United States Government or any agency thereof or its contractors or subcontractors.

PPPL Report Availability

Princeton Plasma Physics Laboratory:

<http://www.pppl.gov/techreports.cfm>

Office of Scientific and Technical Information (OSTI):

<http://www.osti.gov/bridge>

Related Links:

[U.S. Department of Energy](#)

[Office of Scientific and Technical Information](#)

[Fusion Links](#)

NCSX PLASMA HEATING METHODS

H. W. KUGEL* *Princeton Plasma Physics Laboratory, Princeton, New Jersey 08543*

D. SPONG *Oak Ridge National Laboratory, Oak Ridge, Tennessee 37831*

R. MAJESKI and M. ZARNSTORFF *Princeton Plasma Physics Laboratory, Princeton, New Jersey 08543*

Received February 27, 2006

Accepted for Publication March 30, 2006

The National Compact Stellarator Experiment (NCSX) has been designed to accommodate a variety of heating systems, including ohmic heating, neutral beam injection, and radio-frequency (rf). Neutral beams will provide one of the primary heating methods for NCSX. In addition to plasma heating, neutral beams are also expected to provide a means for external control over the level of toroidal plasma rotation velocity and its profile. The experimental plan requires 3 MW of 50-keV balanced neutral beam tangential injection with pulse lengths of 500 ms for initial experiments, to be upgradeable to pulse lengths of 1.5 s. Subsequent upgrades will add 3 MW of neutral beam injection (NBI). This paper discusses the NCSX NBI requirements and design issues and shows how these are provided by the candidate PBX-M NBI system. In addition, estimations are given for beam heating efficiencies, scaling of heating efficiency with machine size and magnetic field level, parameter studies of the optimum beam injection tangency radius and toroi-

dal injection location, and loss patterns of beam ions on the vacuum chamber wall to assist placement of wall armor and for minimizing the generation of impurities by the energetic beam ions. Finally, subsequent upgrades could add an additional 6 MW of rf heating by mode conversion ion Bernstein wave (MCIBW) heating, and if desired as possible future upgrades, the design also will accommodate high-harmonic fast-wave and electron cyclotron heating. The initial MCIBW heating technique and the design of the rf system lend themselves to current drive, so if current drive became desirable for any reason, only minor modifications to the heating system described here would be needed. The rf system will also be capable of localized ion heating (bulk or tail), and possibly IBW-generated sheared flows.

KEYWORDS: *stellarator, neutral beams, radio-frequency heating*

I. INTRODUCTION

The National Compact Stellarator Experiment (NCSX) is designed to accommodate a variety of heating systems, including ohmic heating, neutral beam injection, and radio-frequency (rf) heating. The experimental plan requires ohmic heating and 3 MW of balanced neutral beam injection for initial experiments and provision for subsequent upgrades that could add an additional 6 MW of ICRF and 3 MW of neutral beam injection (NBI).

*E-mail: hkugel@pppl.gov

II. OHMIC HEATING

The ohmic heating capability will be implemented using the poloidal field coils and provides inductive heating up to ± 420 kA of ohmic current. This will be used for initial breakdown and formation of target plasma for neutral beam heating. It will also be used to manipulate the current profile shape, allowing relatively rapid equilibration with the bootstrap current, as discussed in more detail elsewhere.¹

III. NEUTRAL BEAM INJECTION HEATING

The NCSX design will use the PBX-M NBI system consisting of four beamlines with a total injection power

of 6 MW, H^0 at 50 kV for 0.5 s, or 8 MW, D^0 at 50 keV for 0.5 s. The initial configuration will utilize two of the four existing PBX-M neutral beams, one aimed in the codirection and the other in the counterdirection. The design will allow the other two beamlines to be installed in a similar manner as a future upgrade. This section gives a general overview of the NBI system characteristics and the configuration features required by the design.

III.A. Neutral Beam System Characteristics

III.A.1. Available Injection Power

NCSX NBI system will have one ion source per beamline. The ion sources have 30-cm circular copper grids and a focal length of 440 cm. Each ion source was fabricated, tested, and fully qualified at Oak Ridge National Laboratory (ORNL) in 1979–1980 to power levels of 1.5 MW, H^0 (at 50 kV, 100 A, 0.3 s) for the PDX experiment.² In addition, one ion source was demonstrated to yield 2 MW, D^0 (at 50 keV, 70 A, 0.3 s). Subsequent testing after installation on PDX demonstrated the capability to inject 8.3 MW, D^0 with four sources in the absence of magnetic fields. The presence of stray magnetic fields and finite transition duct pressure reduced the available power to 6.5 to 7.0 MW, D^0 . This loss of reionization power of 12 to 18% will be regained in NCSX by reinstalling, in the beamline exit region, the 100 kl/s cryopumping capability of the original ORNL design.

III.A.2. Neutral Species Ratios

NCSX neutral beam design requires high, full-energy, injected neutral power fractions. The PBX-M NBI system meets this requirement. Typical species measurements performed at ORNL with equilibrium density neutralizer cells using ion dump yields found ion source species ratios of $H^0(E):H^0(E/2):H^0(E/3) = 63:20:17$ and neutral beam power output ratios of $P^0(E):P^0(E/2):P^0(E/3) = 80:13:7$ (Ref. 2). On PDX, with D^0 at 47 keV (1.6 MW), using Rutherford backscatter spectroscopy on the injected neutrals found neutral particle ratios of $D^0(E):D^0(E/2):D^0(E/3) = 53:32:15$ and neutral power ratios of $P^0(E):P^0(E/2):P^0(E/3) = 72:21:7$ (Ref. 3).

III.A.3. Pulse Length

The NCSX program plan calls for initial NBI heating pulse lengths of 300 ms, and then extension of the heating pulse lengths to 500 ms. At a later experimental stage, the beamline hardware may be upgraded to accommodate 1.5 to 3 s NBI pulse length capability. The original neutral beamline power-handling surfaces were engineered to operate at a maximum of 500-ms pulse lengths at the full-power peak power density of 3 kW/cm². In addition to power conditioning each of the ion sources at pulse lengths of 300 ms, ORNL in 1979–1980 demonstrated one ion source to operate at 500-ms pulse lengths

using H^0 at about 50 kV, 90 A. Similar results were obtained on PBX-M, with modest changes, where each of the four neutral beamlines was demonstrated to operate with D^0 at ~40 kV, 1 MW, to pulse lengths of 500 ms.

III.A.4. Control and Performance

The NCSX NBI design will use computer control to optimize NBI availability and reliability. In the case of PDX, after NBI installation the project developed full computerization for the NBI system, including control of filament, arc, and acceleration grid conditioning, and fault response using an artificial intelligence or expert rules algorithm.^{4,5} One operator monitored all four systems in a “hands-off” manner. The computer control was found to provide unforeseen benefits in operational reliability, reproducibility, and safety. This software is available and will be ported to a new NCSX-dedicated NBI computer system to facilitate operations.

III.A.5. Ion Source Focal Length, Focusing, and Power Density Profiles

The required NCSX NBI power determines vessel access requirements, since the injected power depends on the effective focal length, focusing, and steering of the output neutral beam. These factors are significant considerations in the design of long, tight transition ducts for tangentially injecting beams.

The PBX-M ion sources consist of three circular grids, 30 cm in diameter, containing about 2000 circular holes for producing 2000 circular beamlets. The grids are shaped spherically concave to provide geometric focusing (aiming) with a focal length of 440 cm, which was the distance to the Poloidal Divertor Experiment (PDX) torus port (Fig. 1). The NCSX NBI alignment will place this focal plane in the narrowest region of the transition duct.

The required grid curvature was modeled using a Gaussian geometric optics code.⁶ Measurements of the respective as-built focal lengths and focusing were performed using a pinhole camera technique and power

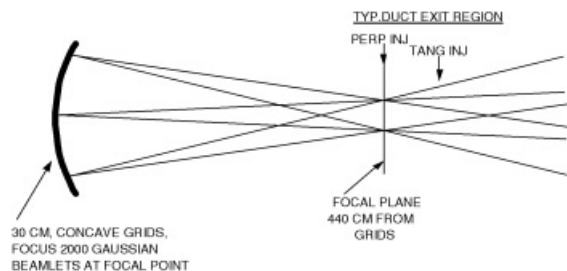


Fig. 1. Schematic of PBX-M ion source grid optics. The ion source grids are curved so as to focus 2000 Gaussian beamlets at a focal point 440 cm from the grids. Ion source optics determine the duct size and achievable aiming angles.

TABLE I
Summary of NBI Optics

NBI System ^a	θ_{HWHM}^b (deg)	W_{HWHM}^c (cm)	$\theta_{\text{HW}1/e}^d$ (deg)	$W_{\text{HW}1/e}^e$ (cm)
S	1.5	11.58	1.8	13.9
E	1.13	8.75	1.36	10.5
NW	1.2	9.25	1.44	11.1
SW	0.94	7.25	1.13	8.7

^aNBI system listed in order of ion source fabrication and testing at ORNL.

^bAngular divergence of beam half-width at half-maximum (HWHW) from centerline to edge.

^cBeam half-width at half-maximum (HWHW) from centerline to edge.

^dAngular divergence from centerline to edge at $1/e$ of full power.

^eBeam half-width from centerline to edge at $1/e$ of full power.

density profile measurements at the focal plane torus target.² The final measured focal lengths were consistent with the design value of 440 cm. Table I gives the H^0 angular divergences for each neutral beam at the torus target horizontal focal plane (440 cm). The results shown in Table I were obtained from measurements of the respective beam power density profiles (Fig. 2) measured

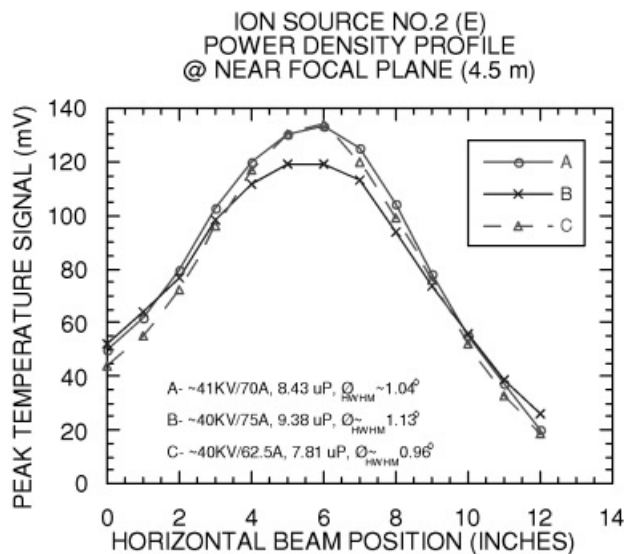


Fig. 2. Power density profile measured at ORNL for PDX ion source 2 (East NBI). It was found that the resultant beam trajectory at the torus target at the exit of the transition duct is not accurately determined by simple, a priori mechanical alignment of the ion source and that measuring the actual beam position in the duct is important for proper beam alignment.

along the horizontal axis in the focal plane at the torus target using a scanning water calorimeter behind pinhole apertures. The results exhibit a Gaussian behavior from peak power density down to about 10% of peak power density. Below the 10% power level, the profiles exhibit “wings” that have been characterized by asymmetric Gaussian or polynomial least-squares fitting.

The NCSX neutral beam configurations and transition duct designs use the above results. The solid and dashed lines in Fig. 3 show the simulated beam power density profile along the beam axis using a Gaussian geometric optics fit to the measurements given in Table I. These power density profiles were used to achieve a duct design that meets the NCSX injected NBI power requirements.

III.A.6. Maximizing Absorbed Power

The NCSX transition duct design, although sufficiently large to accommodate the above power density profiles, also helps to reduce system gas pressure (from the ion source and neutralizer gas flow) in the transition region, which causes reionization, and loss of neutral particles. The subsequent deflection of reionized beam particles into the duct walls by the fringe magnetic field causes additional gas load from outgassing and an avalanching of reionized power loss (~ 2 to 20%, depending on path length and pressure). Maintaining the NCSX NBI transition region neutral gas pressure in about the 10^{-5} torr regime will significantly increase injected power. The NCSX design will accomplish this by optimizing the duct design and by installing additional cryopumping in the front box of the beamline. Table II shows

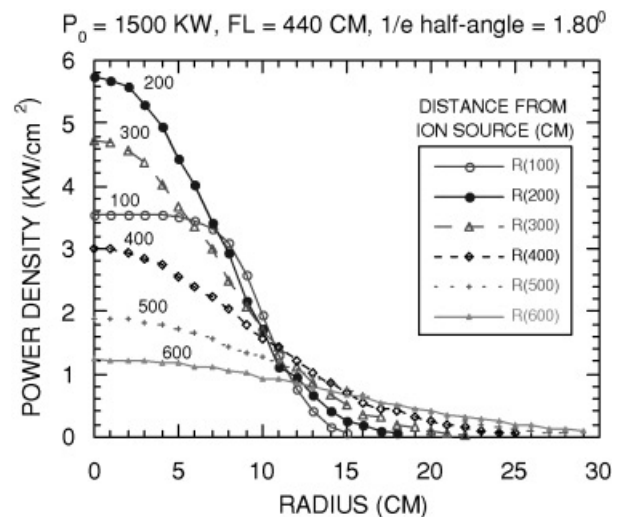


Fig. 3. Simulated power density along beam axis. The beam port location will allow adequate duct width to avoid neutral and reionized power impingement on the duct walls.

TABLE II
NBI Power Capability and Reionization Losses

PBX-M injected power capability
ORNL qualification (no fields)
$H^0 \rightarrow 6 \text{ MW}$ ($4 \times 1.5 \text{ MW}$)
$D^0 \rightarrow 8 \text{ MW}$ ($4 \times 2.0 \text{ MW}$)
PDX testing (no fields)
$D^0 \rightarrow 8.3 \text{ MW}$ (4 NBI at $> 52 \text{ kV}$)
Neutral power reionization loss fractions in PBX-M due to duct neutral gas (~ 1 to $4 \times 10^{-4} \text{ T}$)
Perpendicular ducts $\rightarrow 0.88P_0$ (12% loss)
Tangential ducts $\rightarrow 0.83P_0$ (17% loss)

the NBI system injected power capability and the effects of fringe fields for PBX-M.

III.A.7. Maximizing Desired Neutral Beam Species

The NCSX NBI design goal of maximizing the available NBI power requires maximizing the full-energy-particle component available from the available ion sources. Typically, the PBX-M neutral beam lines were operated with the neutralizer cell at ~ 90 to 95% equilibrium gas pressure to optimize the yield of the full energy component. Section III.A.2 discusses the measured NBI system neutral species yields. NBI system gas from the ion source and neutralizer in the transition duct can change the fractional ionic yield of the low-energy components and produce small differences in the species ratios of injected beam.³ The NCSX design will install additional cryopumping in the front box of the beamline to reduce this effect.

III.A.8. Power Transmission to the Far Wall

The NCSX NBI design includes far-wall armor to provide vessel wall safety without relying entirely on interlocks. Neutral beam power transmission to the far wall of the vessel (“shine-through”) requires at minimum sufficient armor to absorb a short full-power pulse. In PBX-M, this armor was designed to absorb at least a short full-power pulse so as to allow power and position calibration injections in the absence of plasma. Sometimes in PBX-M, this armor was used to absorb short neutral beam-conditioning pulses if the beamline calorimeter was unavailable. Similarly for NCSX, rather than relying completely on either thin armor or no armor, plus interlocks to stop beam injection beyond an acceptable pulse length, the NCSX plan is to achieve a beam armor design capable of stopping a full-power, 0.5-s beam injection in the absence of plasma (e.g., 1.3-cm-thick graphite is an acceptable armor for a 3 kW/cm^2 power deposition for 0.5 s).

Figure 4 shows a plot of the estimated transmission through PDX plasmas versus density for H^0 and D^0 at 40 and 50 keV. These results indicate that, for example, a typical graphite at least 1.3 cm thick or the equivalent will be sufficient for wall armor tiles capable of absorbing the available peak NBI power densities of 3 kW/cm^2 for 500 ms in the absence of plasma, as well as power transmission during plasmas to be encountered in NCSX. Thicker tiles with active cooler would be needed as an upgrade for longer NBI pulse lengths if full-power, full-pulse-length capability are desired for additional vessel safety. The NCSX NBI plan is to install uncooled wall armor tiles, at least 1.3 cm thick, prior to first injection. The actual design will await the completion of other in-vessel hardware.

III.A.9. Minimizing Duct Wall Conditioning

The NCSX NBI design will minimize the time required for transition duct wall conditioning. This procedure is often practiced by high-powered NBI systems using short, low-power pulses prior to the start of high-power-injection operations. Gas absorbed on and in duct walls during nonoperating periods and during operations is released (outgasses) under this particle bombardment and heating. The reduction of strong initial duct outgassing is desirable to prevent “duct choking,” i.e., dangerous reionized power losses. In addition, reduction of daily duct outgassing results in increased injected power and provides more reproducible results. Figure 5 shows the measured PDX East NBI system duct outgassing versus the cumulative power absorbed over several months.⁷ It is seen that initially at the beginning of a 1 to 2 week

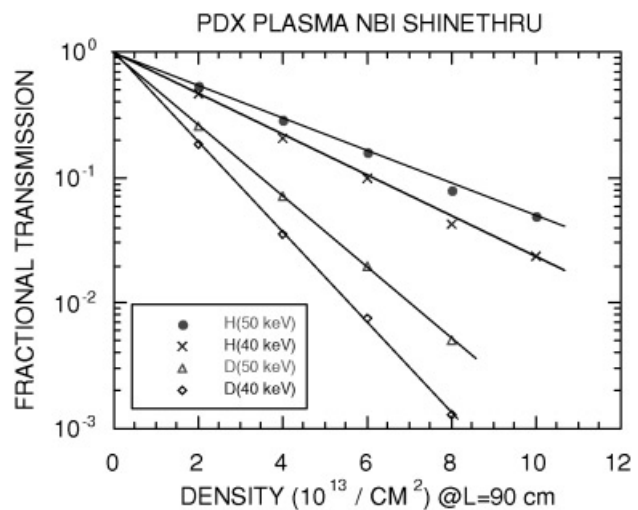


Fig. 4. Plot of neutral beam power fractional transmission through a 90-cm-thick PDX plasma versus density. This corresponds to the case of near-perpendicular injection ($R_{tan} = 35 \text{ cm}$).

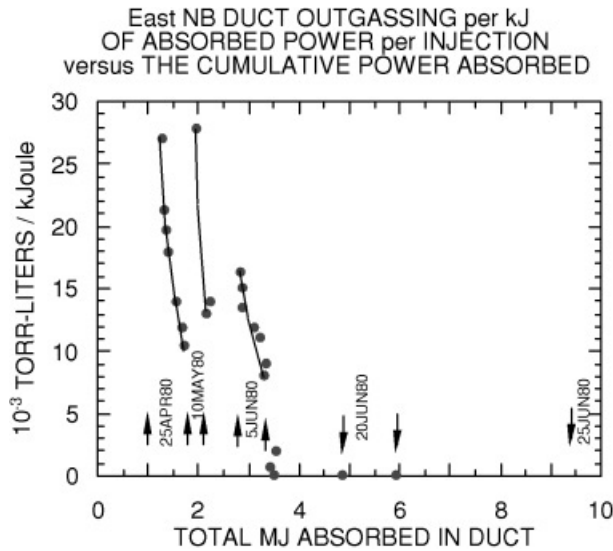


Fig. 5. Measured PDX NBI duct outgassing during several months of operation. H₂ GDC was used to clean the vessel immediately after pumpdown from a vent. No H₂ GDC or other GDC was applied thereafter. The application of He GDC in the transition duct prior to NCSX daily operations and between discharges will reduce duct conditioning time significantly.

experimental campaign, the duct outgassing was high, but it decreased steadily during the experimental campaign. Interruption of the campaign for maintenance resulted in the return of high outgassing rates due to fresh gas absorbed on the duct walls from the vessel and volume diffusion of fresh gas to the surface of the duct walls to replenish the outgassed surface region. The NCSX NBI design will reduce duct outgassing by using high-conductance geometry, with walls far from the beam, appropriate materials, baking, and He glow discharge cleaning (GDC) between discharges. The NCSX design will include the installation of high-speed cryopumping, in the exit box of the beamlines, at the entrance to the duct, to significantly reduce or eliminate the effects of residual duct outgassing. This hardware will also accelerate NCSX pumpdown between discharges.

IV. FAST ION CONFINEMENT ANALYSIS FOR NCSX

IV.A. Introduction

Neutral beams will provide one of the primary heating methods for NCSX; up to 6 MW of beam power will be available in the 40- to 50-keV energy range. These beams will be injected tangentially in both the co- and counterdirections to minimize beam-driven currents. In addition to plasma heating, beams are also expected to provide a means for external control over the level of toroidal plasma rotation velocity and its profile.

NCSX has been designed to be as toroidally symmetric as possible in magnetic Boozer coordinates.⁸ This leads to improved energetic beam ion confinement and higher predicted heating efficiencies in comparison to more conventional stellarators. However, even in such an optimized stellarator, there will remain some nonzero departure from perfect symmetry. These deviations will lead to somewhat enhanced levels of beam ion losses, above those present in an equivalent symmetric tokamak. For example, localized magnetic wells in the stellarator can result in small fractions of locally trapped orbits that drift directly out of the plasma; this ripple can additionally cause banana orbits trapped in the $1/R$ wells to gradually leave the plasma due to the successive perturbations in their bounce points. Barely passing particle orbits are also perturbed by low levels of this ripple; their orbits can become stochastic over many toroidal transits and leave the plasma.

These orbital effects require careful analysis for neutral beam heating since they are especially exacerbated by the nearly collisionless nature and high transit speed of the beam ions. This forms the motivation for the following set of calculations. The model described that follows is used for estimations of beam heating efficiencies (important for plasma performance estimations), scaling of heating efficiency with machine size and magnetic field level, parameter studies of the optimum beam injection tangency radius and toroidal injection location, and loss patterns of beam ions on the vacuum chamber wall (important for placement of wall armor and for minimizing the generation of impurities by the energetic beam ions).

IV.B. Description of Model

Our model (the DELTA5D code⁹) is based on the geometry shown in Fig. 6. A diffuse beam is injected into

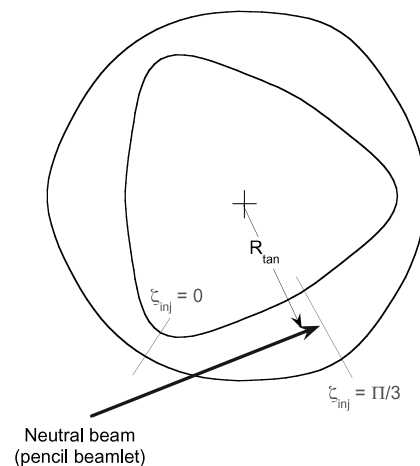


Fig. 6. Geometry used for NCSX neutral beam calculations.

the plasma on the equatorial plane ($\theta = 0$) at a particular toroidal angle ζ_{inj} . The deposition profile for the beam is externally specified and is obtained from the modeling of similar axisymmetric systems (using the cross-sectional shape at the $\zeta = \pi/3$ plane) using TRANSP (Ref. 10). Particles are initially distributed over flux surface locations in consistency with this deposition profile. To determine the initial pitch angle distribution for the beam, a pencil beam model is used. For each beam particle (at flux surface ψ , $\theta = 0$, $\zeta = \zeta_{inj}$), we calculate its major radius R ; initial pitch angles are then determined by the pencil beam relation: $v_{\parallel}/v = R_{tan}/R$. Only flux surfaces having major radii (at $\theta = 0$) $> R_{tan}$ are populated with beam ions. The expectation is that as the beam ions slow down and the pitch angle scatters, they will lose “memory” of their initial conditions in pitch angle θ and ζ and thus not be too sensitive to the model used for these coordinates. Since their losses will be more sensitive to their initial flux surface locations, our model allows that to be determined independently, using a specified diffuse beam deposition profile.

From these initial conditions, the beam particle orbits are then followed by solving Hamiltonian guiding center equations that time advance the particles in the two angular coordinates (poloidal and toroidal angles in Boozer coordinates) and the conjugate momenta. Equilibrium magnetic fields are obtained from the VMEC stellarator equilibrium code,¹¹ which are then transformed to Boozer coordinates.⁸ Collisions with a static background plasma consisting of electrons and two background ion species (a main ion and one impurity com-

ponent) are simulated using a Monte Carlo collision operator¹² based on pitch angle and energy scattering terms, taking into account the full velocity-dependent potentials¹³ without assumptions regarding relative orderings of the electron, beam ion, and impurity velocities. Collisions are allocated on a fixed time step Δt_{coll} , which is chosen so as to maintain $v\Delta t_{coll} \ll 1$ and to allow a smooth granularity in modeling the collisional processes. The time integration step for the orbit integration is controlled by the ordinary differential equation solver LSODE (Ref. 14), which internally chooses an integration time step so as to maintain a prescribed accuracy level. The typical variation of the different beam ion collision frequencies with velocity and flux surface included in this model are shown, in Figs. 7a and 7b, respectively.

The subscripts on the collision frequencies denote the species (electrons, ions, impurities) that the beam is colliding with and whether the collision frequency pertains to pitch angle deflection (D) or energy scattering (E). Currently, we do not include collisions with neutrals. Typically, the beam ions are injected at a velocity at which they are slowing down somewhat more on electrons than ions, but they soon pass through the critical energy, below which they begin slowing down more on ions. Also, as the beam ions pass through the critical energy, pitch angle scattering begins increasing; this can result in higher fast-ion losses as the ions get scattered out of the passing region of velocity space. As the beam ions slow to $\frac{3}{2}kT_{ion}$ (with T_{ion} being the background field ion temperature), they are counted as part of the

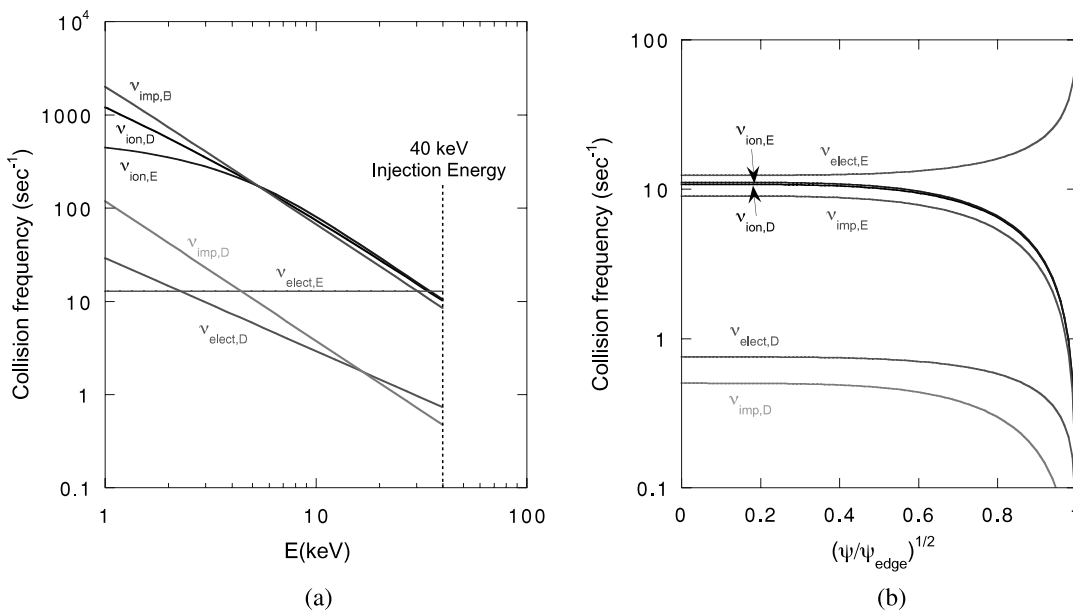


Fig. 7. (a) Collision frequencies versus energy at $r/a = 0.5$ and (b) collision frequencies versus flux surface at $E = 40$ keV. Collision frequencies with D and E subscripts denote pitch angle and energy scattering rates, respectively; *ion*, *elect*, and *imp* subscripts denote beam collisions with plasmas ions, electrons, and impurities.

background plasma species. Beam ions that pass through the outer flux surface are removed from the distribution and not replaced; thus, the quoted loss rates may be a slight overestimated. Beam heating efficiencies are calculated by recording the losses of particles and energy out of the outer magnetic flux surface that occur during the slowing-down process. The DELTA5D code⁹ follows groups of beam particles on different processors in parallel using the MPI language for interprocessor communication. It has been adapted to both the Cray T3E and IBM-SP computers. A variety of diagnostics of the escaping particles, such as pitch angle, energy, and particle lifetime distributions, are retained to aid in understanding the loss mechanisms.

In Fig. 8 we show some of the characteristics of a slowing-down beam for the parameters $n(0) = 8 \times$

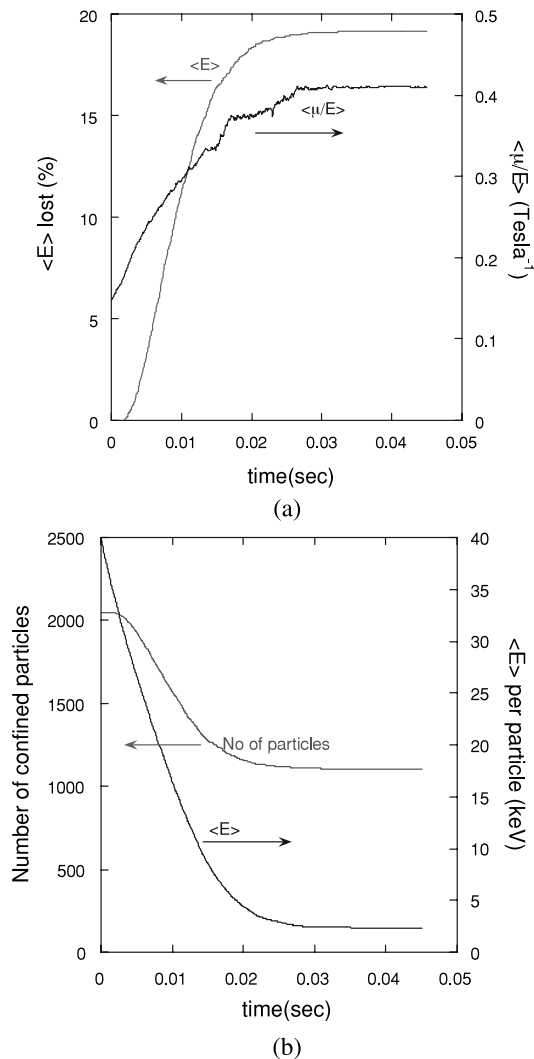


Fig. 8. (a) Typical evolution of ensemble-averaged beam energy loss and $\langle \mu/\epsilon \rangle$. (b) Decay in time of the number of confined beam particles and average energy per particle.

10^{19} m^{-3} , $T_e(0) = 2.9 \text{ keV}$, and $T_i(0) = 2.0 \text{ keV}$. Figure 8a shows on the left-hand scale the time evolution of energy lost from the beam averaged over the ensemble of 2048 particles used here. We normally follow the distribution of beam particles until this energy loss fraction reaches a saturated plateau; this flattening is associated with the average beam ion slowing down to the $\frac{3}{2}kT_{ion}$ energy level (shown on the right-hand scale in Fig. 8b). Figure 8a also shows the time variation of the ensemble-averaged ratio of magnetic moment to energy for the beam. Initially, this ratio starts out small due to the anisotropic nature of the beam (i.e., composed mostly of passing orbits), and then it increases as the beam pitch angle scatters and spreads out to become more isotropic. Finally, Fig. 8b shows the decrease in time of the number of beam particles, indicating the degree to which particles are lost at times prior to that required for slowing down enough to join the background distribution.

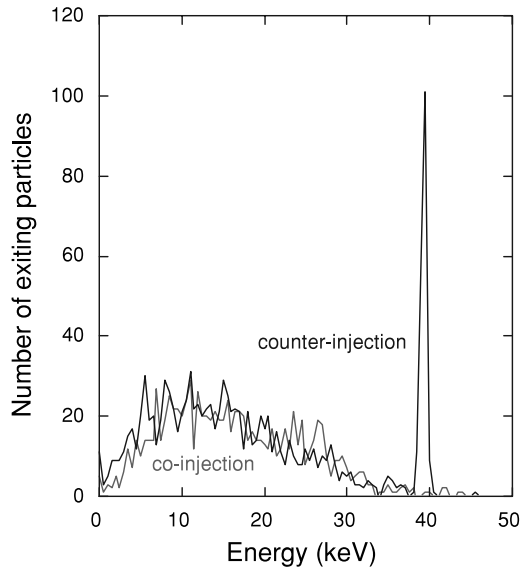
Figures 9a and 9b show histograms of the energy and pitch angle distributions of the escaping beam ions for the case shown in Fig. 8. As can be seen, the energy losses are characterized by a broad peak centered around 15 to 20 keV for both co- and counterinjection. The counterinjected ions also show a very sharp peak at the injection energy, presumably associated with prompt losses.

The pitch angle distributions of escaping ions shown in Fig. 9b are mostly peaked around the deeply trapped range of pitch angles with a secondary peak (for the coinjected ions) more in the transitional region. The counterinjected ions show a very sharp peak near $v_{\parallel}/v = 0.7$ to 0.8 , which is close to the birth pitch angle, indicating a prompt loss component for the case of a tangency radius $R_{tan} = 1.38 \text{ m}$.

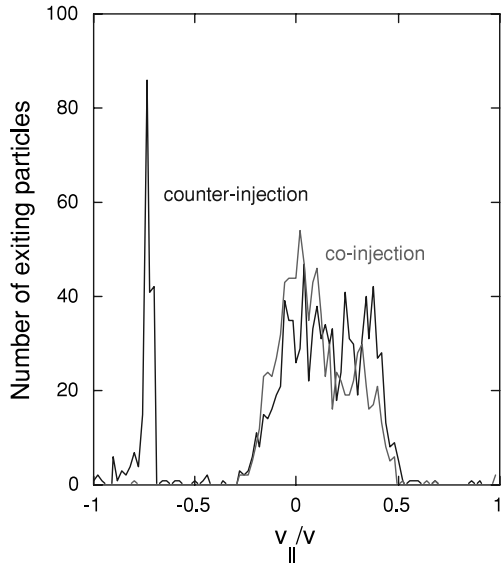
IV.C. Parameter Scans

We have used the model described to study sensitivity to variations in configuration and beam and plasma parameters. In Figs. 10 and 11, we have used the NCSX, M45 configuration,¹⁵ with a volume-averaged magnetic field of 1.6 T, and an average major radius of 1.4 m. The central plasma density is nominally $8 \times 10^{19} \text{ m}^{-3}$, the central ion temperature was 2 keV, and the electron temperature was 2.9 keV; the plasma species is hydrogen. An impurity species is present with $Z = 18$, $A = 9$, at 1% of the electron density, and a temperature equal to the background ion temperature. The beam is also taken as hydrogen and is monoenergetic at injection with an energy of 40 keV. The beam is initially deposited at $\theta_{inj} = 0$, $\zeta_{inj} = \pi/3$. Plasma profiles for temperature and density have been determined from one-dimensional (1-D) transport modeling and the ambipolar potential is set to zero.

In Fig. 10 the tangency radius for injection is varied. As the tangency radius is made smaller, the beams are initially launched onto larger pitch angles relative to the magnetic field (smaller v_{\parallel}/v). This puts them closer to the trapped-passing transitional regime of velocity space,



(a)



(b)

Fig. 9. (a) Energy spectrum and (b) pitch angle spectrum of exiting beam particles.

where orbits are more likely to experience prompt losses. As may be seen, the losses steadily increase for both co- and counterinjected ions as R_{tan} is decreased. The minimum for the counterinjected curve is close to the point where $R_{tan} =$ the magnetic axis location. For this configuration the magnetic axis at the toroidal injection angle ($\zeta_{inj} = \pi/3$) was 1.38 m. As R_{tan} is increased beyond this point, the counterinjected losses again increase due to the fact that the beam ions are progressively being aimed farther out in minor radius, leading to hollow deposition profiles and increased fractions of prompt orbit losses.

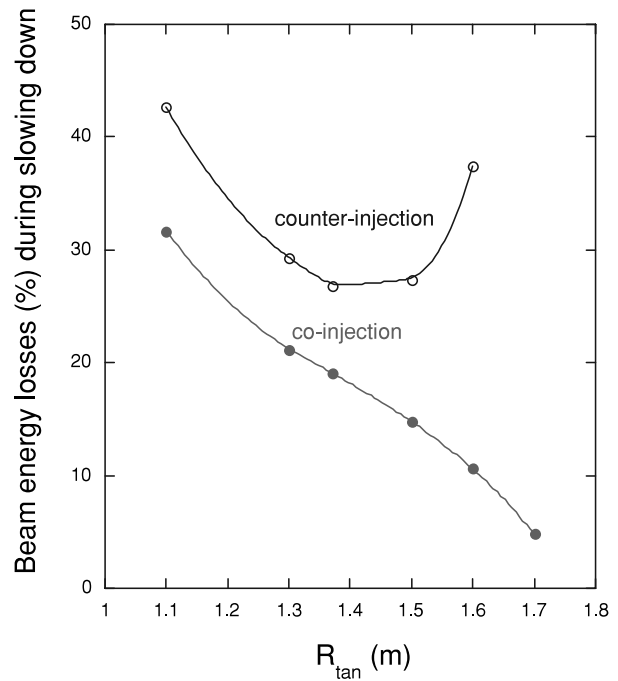


Fig. 10. Dependence of beam losses on beam tangency radius for a version of NCSX with $R_0 = 1.4$ m.

The co-injected losses continue to decrease as R_{tan} is increased beyond the magnetic axis location. This results for several reasons. First, as R_{tan} is increased, the pitch angle distribution of the beam becomes increasingly aligned with the magnetic field (i.e., near $v_{||}/v = 1$) and thus farther from the lossy trapped-passing region. Also, the beam distribution becomes more localized to the plasma edge; for the profiles of temperature and density used here, the slowing down time is shorter near the edge. More rapid slowing down results in lower losses for the beam ions since they spend less time at high energies, where losses are larger. Finally, for co-injected beams the prompt losses are low, so the nearness of the beam to the plasma edge does not enhance losses to the extent that it does for counterinjected beams. The main issue that needs to be resolved as R_{tan} is increased for co-injected beams is how this affects the heating deposition profile. At some point this may become too hollow to be of interest.

In Fig. 11 we examine the variation of beam losses as the magnetic field is changed, using 40-keV beams. As can be seen, there is a monotonic decrease in beam losses with increasing magnetic field strength, with counterinjected losses being larger than co-injected losses. Figures 12 and 13 show the pitch angle and energy spectra of the escaping beam ions as the magnetic field strength is varied.

As indicated in Fig. 9a, a large fraction of the escaping beam ions leave the plasma with one-third to one-half of their initial injection energy. It is desirable to intercept

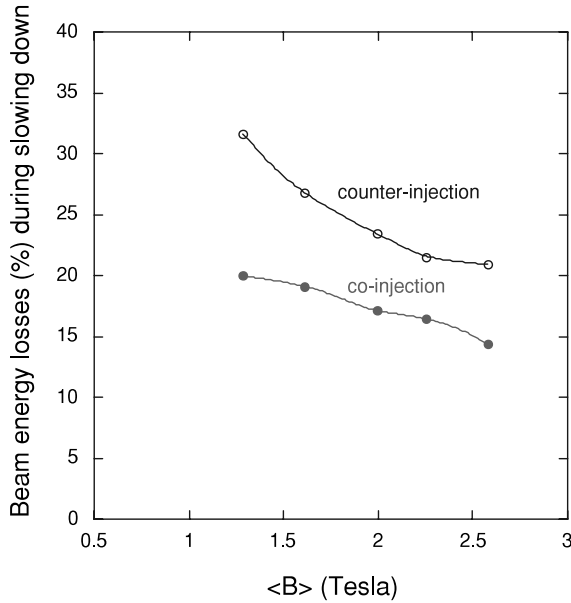


Fig. 11. Variation of beam losses with magnetic field for 40-keV hydrogen ions for a device with $R_0 = 1.4$ m.

this power deposition on the vacuum chamber wall by localized protective armor plating to minimize impurity generation and wall erosion. To design such structures, it is necessary to make estimates of the wall locations where the escaping beam ions will be deposited. As a first step toward such estimates, as the beam ions leave the outermost closed flux surface, we record their exit locations, exit times, pitch angles, and energies. It should be noted that these are only the loadings at the outer flux surface and may not reflect the distributions of lost ions at the vacuum chamber wall. More realistic models will need to be developed that follow the fast ion trajectories in the outer region, where flux surfaces no longer exist. Results at the outermost flux surface based upon the current model are shown in Figs. 14 and 15 for a typical case. Here the exit locations are plotted in Boozer poloidal and toroidal angle coordinates. These losses are superimposed on contours of $|B|$ and magnetic field lines. The fast ion losses are primarily concentrated in helical stripes following the field lines on the bottom of the stellarator, with one stripe per field period. In the case of counterinjected beams, there are also some losses (possibly prompt) near the inboard region of the torus ($\theta \sim \pi$).

Finally, we have plotted the ion loss locations on the three-dimensional (3-D) outermost flux surface (Fig. 16) as obtained from the VMEC stellarator equilibrium code. Exit positions for both co- and counterinjected beam ions are indicated. Again, it can be seen that the losses are somewhat concentrated, motivating the design of protective structures at these locations. These issues are further discussed elsewhere.¹⁶

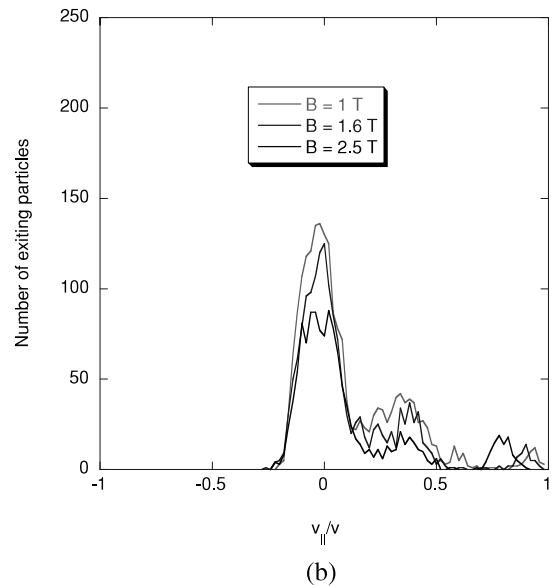
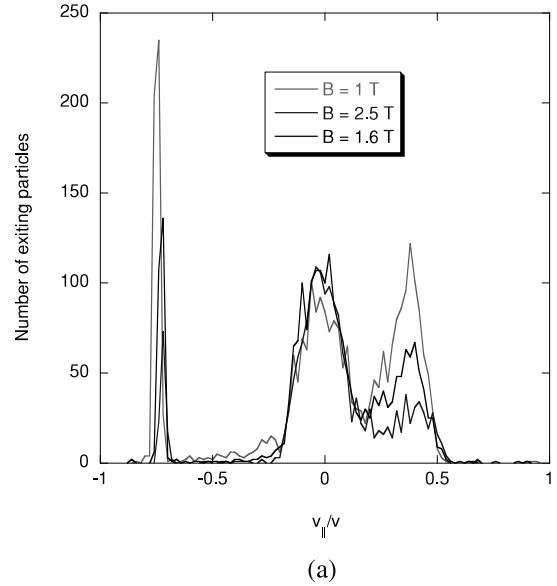


Fig. 12. Pitch angle spectrum of (a) counterinjected and (b) co-injected losses as magnetic field is varied.

IV.D. Suggestions for Future Work

The model described here has been developed for comparative studies of different NCSX configurations and to obtain approximate estimates of beam heating efficiencies and loss patterns. To develop an adequate physics understanding of fast ion confinement in a real experiment, a number of upgrades and new tools will need to be developed. Although many of these issues have already been thoroughly examined for tokamaks, the inherently 3-D nature of the stellarator geometry will, in many cases, require a complete redevelopment of existing tools.

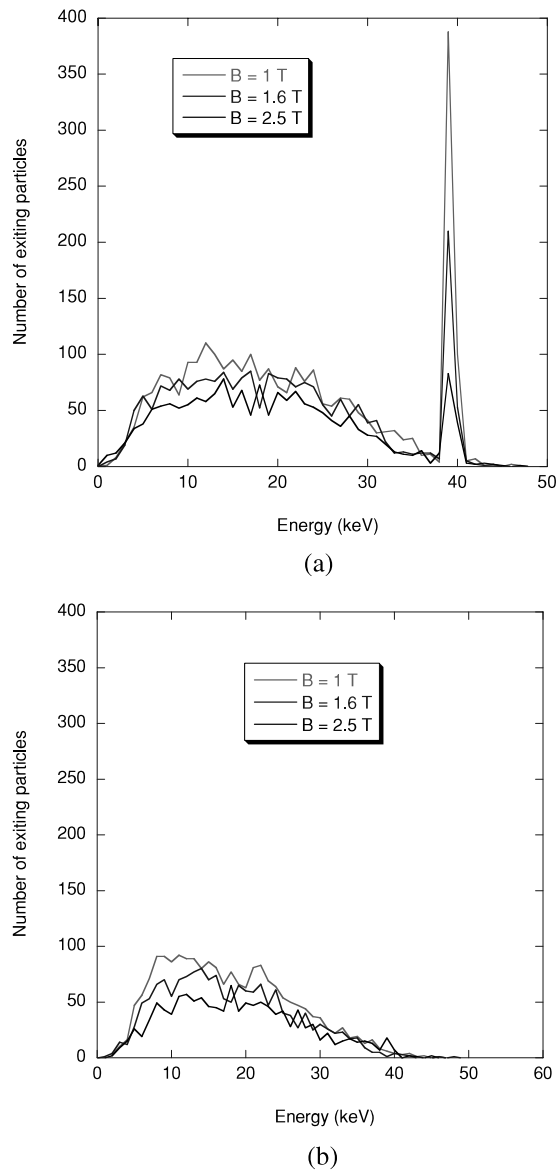


Fig. 13. Energy spectrum of (a) counterinjected losses and (b) coinjected losses as magnetic field is varied.

In the area of neutral beam deposition, finite width, multiple energy group beam models will need to be developed and their intersection with the 3-D flux surface shapes taken into account. As the beam ions slow down, collisions with neutrals and multiple impurity species should be modeled; beam-beam self-collisions and finite beam gyroradius effects may also be of relevance for some regimes. A number of additional physics diagnostics for beam ion effects can readily be included in the Monte Carlo calculations. For example, beam-driven currents and transfer rates of beam energy to the different plasma species can be obtained. Other diagnostics, such as predictions of the energy distributions of charge exchange neutrals escaping the plasma, can be useful in interpreting charge exchange measurements.

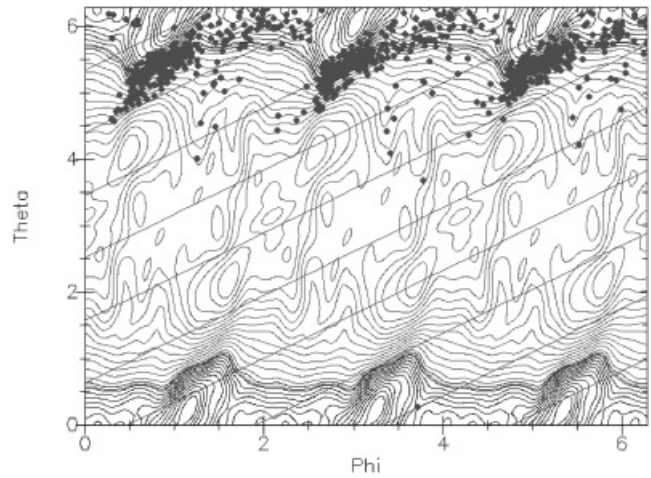


Fig. 14. Locations of coinjected beam losses (dots) on outer surface in two-dimensional Boozer coordinates with $|B|$ contours (wavy lines) and magnetic field lines (straight lines) shown.

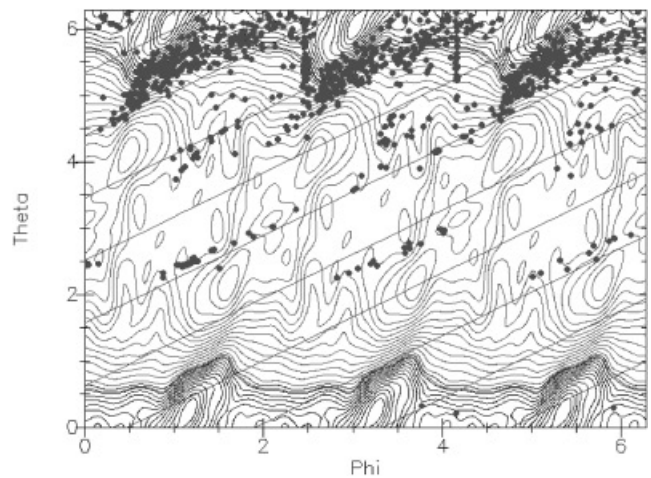


Fig. 15. Locations of counterinjected beam losses (dots) on outer surface in two-dimensional Boozer coordinates with $|B|$ contours (wavy lines) and magnetic field lines (straight lines) shown.

The beam slowing-down model described here assumes nested, closed flux surfaces. Stellarators can develop magnetic islands and open field lines at some point near the plasma edge. In determining beam loss rates through these regions as well as beam loss patterns and heat loads on walls and divertors, it could be important to follow beam ion orbits into these regions by matching together Hamiltonian orbit models for the inner closed surface region with more conventional real-space guiding center drift models for the regions outside the last closed flux surface.

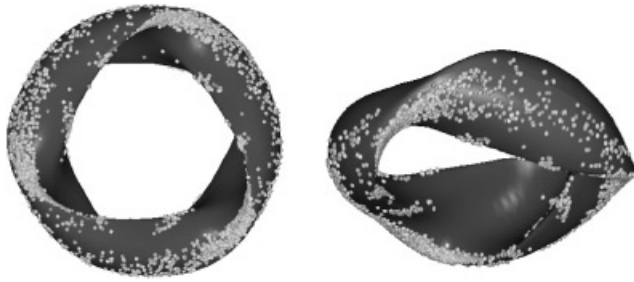


Fig. 16. Location and energy spectrum of co- and counter-beam losses on outer surface in three dimensions.

V. RADIO-FREQUENCY HEATING

V.A. Introduction

The rf heating system for NCSX will be designed to deliver 6 MW of rf power to the plasma. The primary requirement is for electron heating, since the NBI system is expected to provide ion heating. At present, there is no projected need for current drive capability in order to cancel residual currents driven by neutral-beam injection during unbalanced injection, or to further tailor the equilibrium. However, the chosen rf heating technique and the design of the rf system lend themselves to current drive, so if current drive became desirable for any reason, only minor modifications to the heating system described here would be needed. The rf system will also be capable of localized ion heating (bulk or tail), and possibly ion Bernstein wave (IBW)-generated sheared flows.

The rf heating technique chosen for NCSX is mode conversion ion Bernstein wave (MCIBW) heating. NCSX is designed to accommodate high-harmonic fast-wave and electron cyclotron heating as possible future upgrades. However, such systems are not planned at this time.

VI. MODE CONVERSION RF HEATING

VI.A. Introduction

In MCIBW a fast magnetosonic wave, excited at the boundary of a multiple-ion species plasma, propagates to the ion-ion hybrid layer, where it undergoes conversion to the slow wave. Typically, the damping lengths for the slow IBWs are many times shorter than those for the launched fast wave, so power deposition occurs in a highly localized region near the hybrid layer. When the ion temperature is modest and the species mix is such that mode conversion takes place far from an ion cyclotron resonance, the IBW damps on electrons. For high ion tem-

peratures or modest concentration of one of the ion species so that the mode conversion layer is located close to a cyclotron resonance, ion damping can be produced.

Mode conversion heating was first successfully demonstrated using a high-field-side launch in the Tokamak Fontenay-aux-Roses.¹⁷ Efficient, localized electron heating using mode conversion was predicted¹⁸ and demonstrated¹⁹ in the Tokamak Fusion Test Reactor (TFTR) and more recently has been extensively utilized in Alcator C-Mod (Ref. 20). In tokamaks, a low-field-side launch of the fast wave in D-³He has been most commonly employed. The choice of a low-field-side launch is primarily by available hardware and the difficulties inherent in positioning antennas on the high-field-side of a tokamak. Mode conversion with a high-field-side launch, which is very efficient with a wider variety of ion species mixes, has now been utilized successfully in the LHD (Ref. 21), WVII-AS (Ref. 22), and CHS (Ref. 23) stellarators. Modeling of NCSX plasmas has indicated that a high-field-side fast-wave launch is necessary to efficiently access the mode conversion regime. Although such a launch would have been exceedingly difficult or impossible to accommodate with the original saddle-coil design for NCSX, the modular coil design will permit installation of a high-field-side antenna. The antenna will be constructed with a relatively small radial build, which lends itself to installation in a shallow “pocket” in the vacuum vessel, on the high-field side.

The METS 95 code, a 1-D hot plasma full-wave code that has been extensively benchmarked during mode conversion heating experiments in TFTR and C-Mod, has been employed to model mode conversion in NCSX. Mode conversion scenarios for NCSX have now been identified for D-H and D-³He plasmas. Either ion or electron heating can be selected through an appropriate choice of the species mix and launched wave number.

VI.B. Mode Conversion in D-H

The results of modeling D-H mode conversion are shown in Fig. 17. Figure 17a is a plot of the dispersion relation for 10% H in a D-majority plasma, with a central magnetic field of 1.6 T, a central electron density of $5 \times 10^{19} \text{ m}^{-3}$ (parabolic profile), for a fast wave excited at 20 MHz with a wave number of 9 m^{-1} . Ionic species concentrations are given as (n_{ion}/n_e) . Note that this and all following modeling is largely invariant in (ω/Ω_i) ; if operation at a lower (higher) magnetic field is desired, then the launch frequency must be reduced (increased).

For the ion and electron temperatures chosen ($T_e = T_i = 1 \text{ keV}$), METS 95 indicates that majority D/minority H mode conversion will produce relatively weak absorption, with a broad deposition profile on the electron population. Since absorption occurs well to the high-field side of the hydrogen cyclotron resonance, a relatively high magnetic field is required to obtain core heating with this mode conversion scenario.

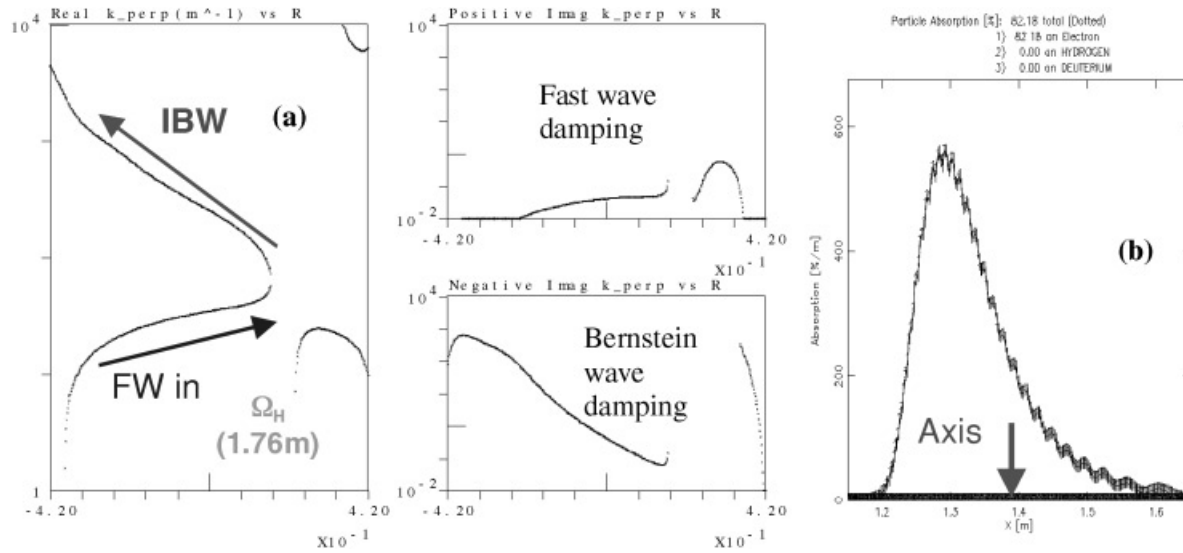


Fig. 17. (a) Dispersion relation for mode conversion in 10% H, 90% D in NCSX and (b) power deposition profile. Eighty-two percent of the launched power is deposited on electrons within the simulation window, with a full-width at half-maximum of ~ 15 cm. The central density for the simulation was $5 \times 10^{19} \text{ m}^{-3}$ (parabolic profile), central $T_e = T_i = 1$ keV, and 1.6 T, with a launched frequency of 20 MHz and wavenumber of 9 m^{-1} .

Although the option to use hydrogenic plasmas would permit access to possible low-recycling regimes, operation at the lower toroidal field initially available on NCSX with core heating would require a prohibitively low operating frequency (~ 15 MHz). Finally, lower hydrogen concentrations ($\sim 5\%$) would allow experiments in conventional light ion minority heating, although the fast ion tail population may not to be well confined in NCSX.

VI.C. Mode Conversion in H- ^3He

The most promising and flexible ion system for mode conversion heating in NCSX is H- ^3He , which should permit localized ion or electron heating (or electron current drive), either on or off axis. With a transmitter frequency of 20 MHz [the lowest practical frequency for the existing Princeton Plasma Physics Laboratory (PPPL) sources], on-axis heating can be obtained at central magnetic fields as low as 1.3 T.

Localized electron heating can be produced in H- ^3He for a wide range of species mixes and wave numbers. In Fig. 18a we display a dispersion relation computed for NCSX with 25% ^3He in hydrogen, for 20 MHz excitation at 1.5 T central magnetic field. The dispersion relation for the IBW indicates that k_{\perp} increases rapidly as the wave propagates away from the ion-ion hybrid layer, back toward the high-field side. Localized electron damping results, as shown in Fig. 18b. However, ion heating is predicted for low concentrations of either hydrogen (light ion minority) or helium (heavy ion minority). In Fig. 19 the dispersion relation and deposition profile for 10% ^3He in H are shown. Deposition is predicted to be pri-

marily on the ^3He population. To produce ion heating, it is necessary to launch the fast wave at high wave number (12 m^{-1}) to obtain Doppler-broadened Bernstein wave damping on the helium. In this case generation of an ion tail is not likely, since a larger (10%) minority ion population is heated and since ^3He tail formation requires higher power densities and smaller minority populations than hydrogen minority heating.

Since the fast wave is mode converted to an IBW that subsequently damps on ions at the cyclotron resonance, it may be possible to generate sheared flow²⁴ with this heating technique. Note that if deposition at the $\frac{2}{3}$ radius is desired (to increase the core plasma volume bounded by the shear flow layer), then the magnetic field can be reduced to 1.5 T. Note also that the deposition layer (at least in this 1-D model) is extremely narrow, with a full-width at half-maximum of only ~ 1 cm.

These capabilities (localized or broad electron heating, localized current drive or current profile control, localized ion heating, possible rf shear flow drive) combine to make mode conversion heating an attractive physics tool for NCSX.

VII. RF SYSTEMS AND ANTENNAS FOR MODE CONVERSION

VII.A. RF Systems

The existing PPPL Fusion Materials Irradiation Test (FMIT) units could be used for mode conversion heating

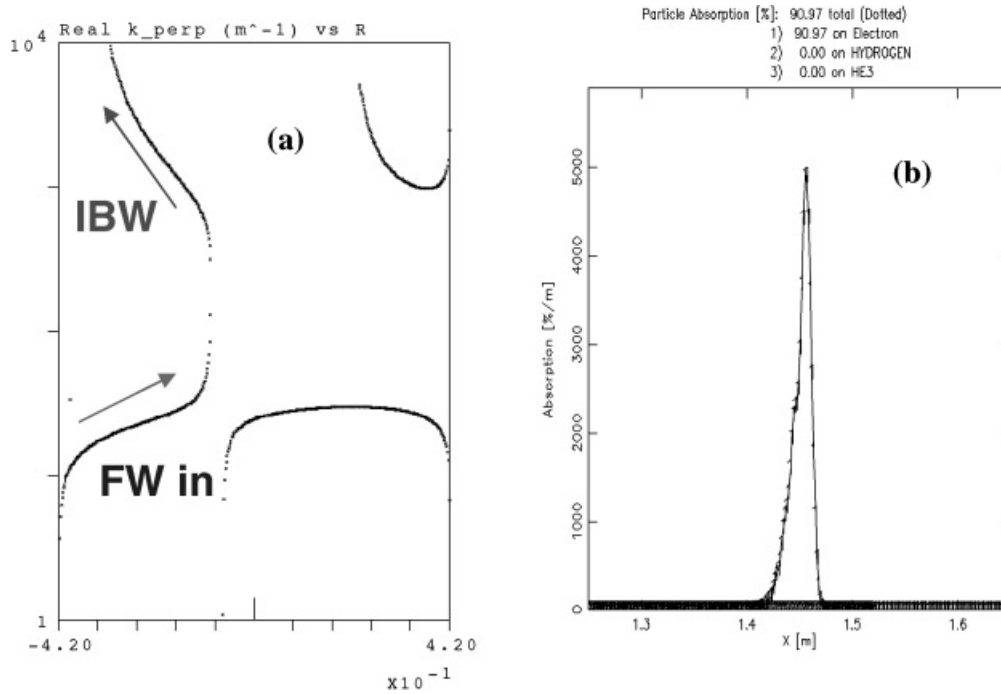


Fig. 18. (a) Dispersion relation for mode conversion in 50% H, 25% ^3He plasmas. The excited frequency is 20 MHz at a wave number of 10 m^{-1} , with a central magnetic field of 1.6 T, central density of $5 \times 10^{19}\text{ m}^{-3}$ (parabolic profile), and central $T_e = T_i = 1\text{ keV}$. (b) Ninety percent of the launched rf power is absorbed on the electrons in a single pass.

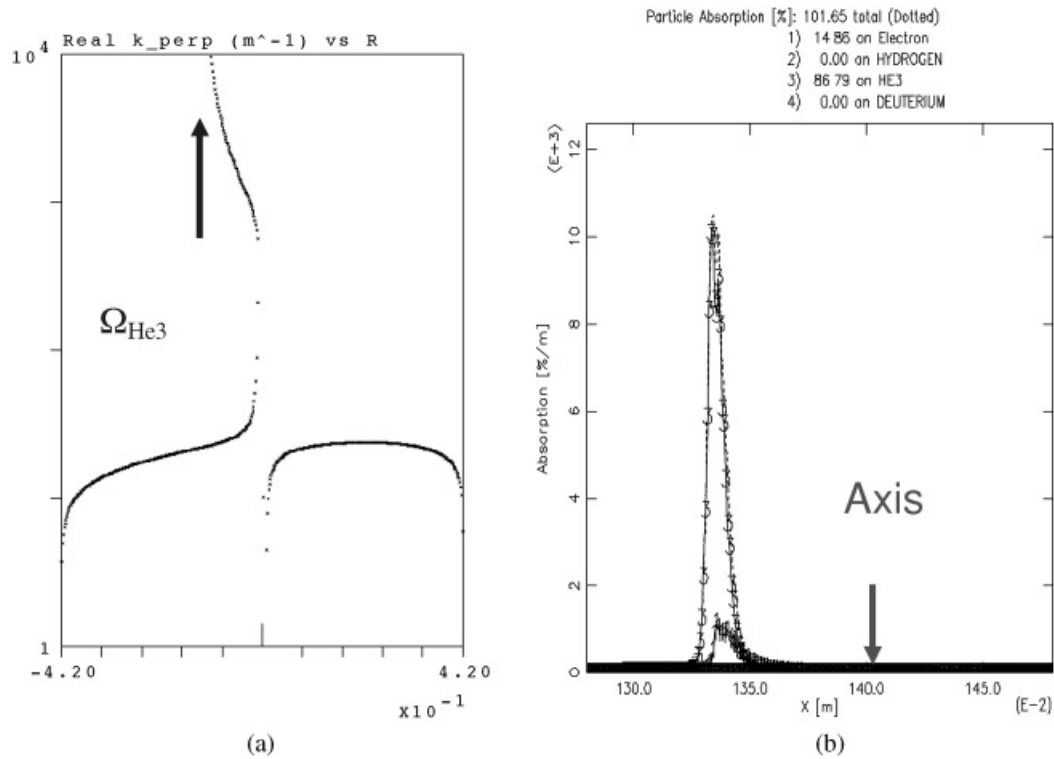


Fig. 19. (a) Dispersion relation and (b) power deposition profile for mode conversion in 10% ^3He , 80% H at 1.8 T, 20 MHz, launched wave number of 6 m^{-1} , central density of $1 \times 10^{20}\text{ m}^{-3}$, and 1.0-keV ion and electron temperatures.

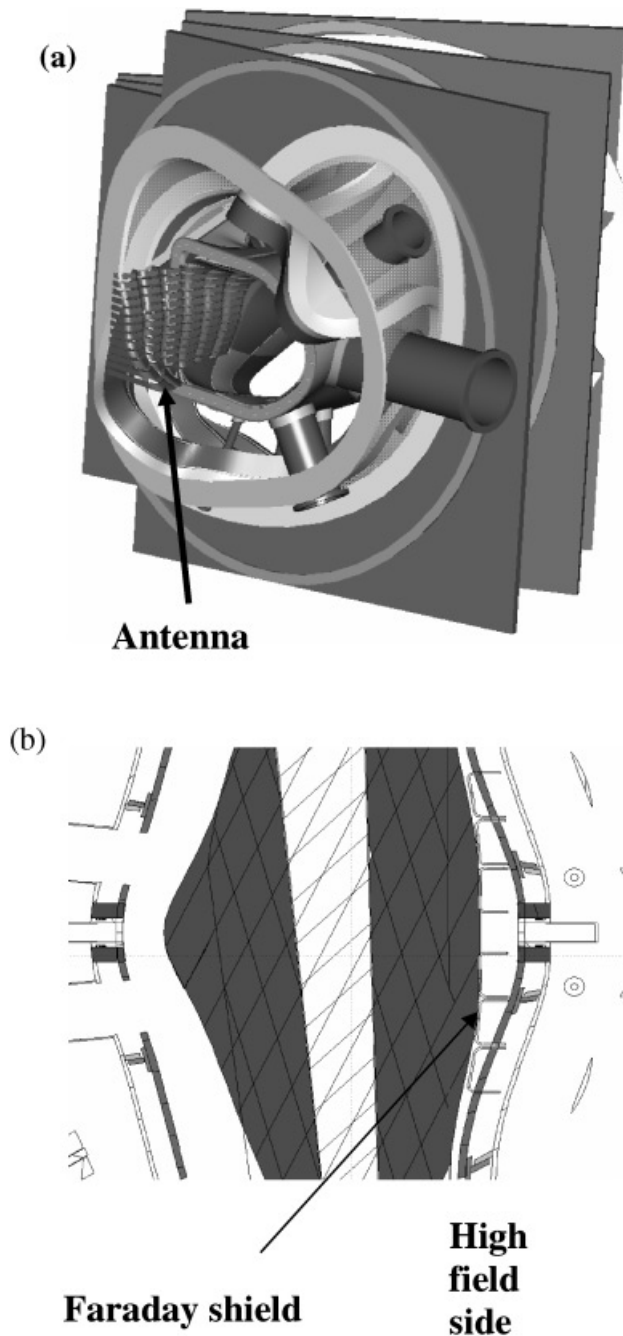


Fig. 20. (a) Cutaway view of NCSX showing the high-field-side antenna. (b) Midplane cut through the NCSX vessel showing the rf antenna Faraday shields and the plasma shape.

in NCSX, in a time-sharing arrangement with the National Spherical Torus Experiment (NSTX). An engineering study has determined that operation of two of the four FMIT sources over the frequency range of 20 to 30 MHz is feasible; this would provide 4 MW of rf source power. An additional 3 to 4 MW would be available from the

remaining two sources, depending on the degree to which they were reconfigured. Although the sharing of sources precludes simultaneous rf heating of NSTX and NCSX, the transmitter modifications proposed would require minimal down time to change frequencies. A changeover from the NSTX operating frequency of 30 MHz to one of the NCSX operating frequencies (or the reverse) is expected to take a few days.

VII.B. Antennas

The vacuum vessel design will accommodate three six-strap antennas, with each antenna installed in a recess in the vacuum vessel on the high-field side. The depth of the recess varies from 9 to 16 cm deep, with a toroidal extent of 90 cm and a poloidal extent of 37 cm. Each antenna is required to couple 2 MW of rf power, so the design power density at the antenna face is approximately 600 W/cm^2 , which is in the range of the JET and NSTX experiments. Each of the six straps will be fed through 4-in. coax. Accommodation for the 4-in. feed lines has been made in the vacuum vessel design (see Fig. 20). The straps will be driven single ended (grounded at one end), and the Faraday shields and straps will be conformal to the plasma boundary.

The external matching system has not yet been designed. At present an externally coupled comb-line system is favored. Further modeling will be required to design a comb-line system tunable over the 20- to 30-MHz frequency range.

Although the final antenna design will incorporate six straps, initial installation of two straps at a single antenna location is planned in order to assess coupling and matching circuit requirements. Initial operation will utilize very low-power sources for coupling studies in a later phase of NCSX. A short-pulse transmitter with 500-kW output is available on-site for initial experiments. With a 500-kW source, the power coupled per strap (250 kW) will be comparable to the design value (330 kW).

ACKNOWLEDGMENT

This work is supported by the U.S. Department of Energy, contracts DE-AC02-76CH03073 and DE-AC05-00OR22725.

REFERENCES

1. E. A. LAZARUS et al., "Simulation of a Discharge for the NCSX Stellarator," *Fusion Sci. Technol.*, **46**, 209 (2004).
2. W. L. GARDNER et al., "The ORNL Prototype PDX Neutral Beam Injection System," *Proc. 8th Symp. Engineering Problems of Fusion Research*, San Francisco, California, November 13–16, 1979, p. 972 (1979).

3. H. W. KUGEL et al., "Neutral Beam Species Measurements Using in situ Rutherford Backscatter Spectroscopy," *Rev. Sci. Instrum.*, **56**, 1105 (1985).
4. T. A. KOZUB et al., "A New Hardware and Software Configuration for the PBX-M Neutral Beam Computer System," *Proc. 12th Symp. Fusion Engineering Research*, Monterey, California, October 1987, p. 606 (1987).
5. K. TUTTLE-FRANK et al., "A Rule-Based Computer Control System for PBX-M Neutral Beams," *Proc. 12th Symp. Fusion Engineering Research*, Monterey, California, October 1987, p. 596 (1987).
6. J. KIM and J. WHEALTON, "Beam Intensity Distributions in Neutral Beam Injection Systems," *Nucl. Instrum. Methods*, **141**, 187 (1977).
7. H. W. KUGEL et al., "PDX Neutral Beam Reionization Losses," *J. Vac. Sci. Technol.*, **20**, 4, 1197 (1982).
8. A. H. BOOZER, "Plasma Equilibrium with Rational Magnetic Surfaces," *Phys. Fluids*, **24**, 1999 (1981).
9. D. A. SPONG et al., "Heating, Energetic Particle Confinement, and Transport in Compact Stellarators," *Bull. Am. Phys. Soc.*, **44**, 215 (1999).
10. R. V. BUDNY, D. C. McCUNE, M. H. REDI, J. SCHIVELL, and R. M. WIELAND, "TRANSP Simulations of International Thermonuclear Experimental Reactor Plasmas," *Phys. Plasmas*, **3**, 4583 (1996).
11. S. P. HIRSHMAN and J. . WHITSON, "Steepest-Descent Moment Method for Three-Dimensional Magnetohydrodynamic Equilibria," *Phys. Fluids*, **26**, 3553 (1983).
12. A. H. BOOZER and G. KUO-PETRAVIC, "Monte Carlo Evaluation of Transport Coefficients," *Phys. Fluids*, **24**, 851 (1981).
13. S. P. HIRSHMAN and D. J. SIGMAR, "Approximate Fokker-Planck Collision Operator for Transport Theory Applications," *Phys. Fluids*, **19**, 1532 (1976).
14. A. C. HINDMARSH, "Odepack, A Systematized Collection of ODE Solvers, in Scientific Computing," pp. 55–64, R. S. STEPLEMAN et al., Eds., North-Holland, Amsterdam (1983).
15. M. ZARNSTORFF et al., "Physics of the Compact Advanced Stellarator NCSX," *Plasma Phys. Control. Fusion*, **43**, A237 (2001).
16. P. K. MIODUSZEWSKI et al., "Power and Particle Handling and Wall Conditioning in NCSX," *Fusion Sci. Technol.*, **51**, 238 (2007).
17. EQUIPPE TFR, *Proc. 9th Int. Conf. Plasma Physics and Controlled Nuclear Fusion Research*, Baltimore, Maryland, Vol. 2, p. 17 (1982).
18. R. MAJESKI et al., "Electron Heating and Current Drive by Mode Converted Slow Waves," *Phys. Rev. Lett.*, **73**, 2204 (1994).
19. R. MAJESKI et al., "Mode Conversion Heating and Current Drive Experiments in TFTR," *Phys. Rev. Lett.*, **76**, 764 (1996).
20. P. T. BONOLI et al., "Mode Conversion Electron Heating in Alcator C-Mod: Theory and Experiment," *Phys. Plasmas*, **7**, 1886 (2000).
21. T. WATARI et al., "The Performance of ICRF Heated Plasmas in LHD," *Nucl. Fusion*, **41**, 325 (2001).
22. D. A. HARTMANN et al., *Proc. 17th Conf. Fusion Energy*, Vol. 2, p. 575, C&S Papers Series 1/p, International Atomic Energy Agency, Vienna, Austria (1999).
23. S. MASUDA et al., "Strong Electron Heating in CHS ICRF Heating Experiments," *Nucl. Fusion*, **37**, 53 (1997).
24. J. R. WILSON et al., "Ion Cyclotron Range of Frequencies Heating and Flow Generation in Deuterium-Tritium Plasmas," *Phys. Plasmas*, **5**, 1721 (1998).

The Princeton Plasma Physics Laboratory is operated
by Princeton University under contract
with the U.S. Department of Energy.

Information Services
Princeton Plasma Physics Laboratory
P.O. Box 451
Princeton, NJ 08543

Phone: 609-243-2750
Fax: 609-243-2751
e-mail: pppl_info@pppl.gov
Internet Address: <http://www.pppl.gov>